To appear in *Vehicle System Dynamics*
Vol. 00, No. 00, Month 20XX, 1–19

A three-dimensional free-trajectory quasi-steady-state optimal-control method for minimum-lap-time of race vehicles

S. Lovato and M. Massaro*

Department of Industrial Engineering, University of Padova,
Via Venezia 1, 35131 Padova, Italy

(*Received 00 Month 20XX; accepted 00 Month 20XX*)

A method to solve minimum-lap-time problems using quasi-steady-state models and free (i.e. not predetermined) trajectory on two-dimensional tracks has been recently proposed. This work describes the extension of the method to three-dimensional tracks and builds upon g-g-g diagrams (instead of the standard g-g), to account for the effects of three-dimensionality. The main features of car and motorcycle g-g-g diagrams are discussed, to get insight into the main effects of three-dimensionality and to suggest a convenient parametrisation for the subsequent optimal control problem (OCP), whose size is not affected by the complexity of the vehicle model employed to generate the g-g-g diagrams. The application of the method to the Mugello and Barcelona-Catalunya circuits is given, with vehicle datasets resembling those of a race motorcycle (MotoGP) and a race car (Formula One). The results obtained are in line with those reported in the literature using full-dynamic models, yet such dynamic models are generally associated to the solution of much larger OCP.

Keywords: minimum-lap-time; three-dimensional road; free-trajectory; quasi-steady-state; g-g map; MotoGP; Formula One; cars; motorcycles; Mugello; Barcelona-Catalunya circuit.

1. Introduction

Minimum-lap-time problems have been historically solved by employing quasi-steady-state models on a predetermined (fixed) trajectory, see e.g. [1–9], or by employing dynamic models on a free (i.e. not predetermined) trajectory, see e.g. [10–27]. The latter approaches usually involve the solution of a nonlinear-optimal-control problem (OCP), either through direct or indirect methods [28, 29].

A third approach, where the minimum-lap-time problem is solved using quasi-steady-state models and free trajectory on two-dimensional tracks, has been recently proposed in [30]. The advantage is that the complexity of the problem is confined to the calculation of the g-g maps, while the related OCP remains simple, since the solver only observes the shape of the g-g diagrams and not the model behind it. In addition, g-g maps are often readily available because they are computed for other purposes, e.g. to compare different vehicle set-ups. Finally, since the selected maps may be representative of a car, a bike or some other road vehicle, the approach is quite general.

The aim of the current work is to devise a three-dimensional free-trajectory minimum-time method based on quasi-steady-state models. The method is the natural extension

---

*Corresponding author. Email: matteo.massaro@unipd.it of [30] to the more general three-dimensional scenarios. The tracks are modelled using curvilinear coordinates, which has proven to be an effective approach when dealing with OCP problems of road vehicles [28, 29, 31]. Semi-analytical g-g-g diagrams for a car and a motorcycle are also derived for a number of reasons: to get insight into the three-dimensional issues, to derive a suitable set of coordinates for the OCP problem, to provide the basis for the example of applications of the methods. However, the methods discussed still work if such semi-analytical diagrams are replaced by those derived from a more complex numerical model or even from experiments. The Mugello and Catalunya tracks are considered because their geometry is available from the literature [26, 27, 31].

The work is organised as follows. In Sec. 2 the road modelling and vehicle positioning are described. In Sec. 3 the g-g-g maps of a motorcycle and a car are derived and key points highlighted. In Sec. 4 the OCP problem is formulated. In Sec. 5 examples of application are given and the results compared against those in the literature.

2. Road model and vehicle positioning

The three-dimensional road modelling and vehicle positioning are tackled with curvilinear coordinates. The approach has been already described and employed in a number of places including [28, 29, 31]. Therefore, only the essential relationships are given below.

The road centreline is defined using its curvature κ and torsion τ, which are given as a function of the travelled distance along the road, i.e. the curvilinear coordinate s. The road plane is created by adding width w and twist ν to the road centreline. A moving trihedron, called Darboux frame, moves with the vehicle along the centreline and its $x-y$ plane represents the road tangent plane. The orientation of such frame is expressed using the attitude-slope-banking convention. The related angles, θ-μ-ϕ, are obtained by integration of κ, τ and ν or alternatively by integration of the relative torsion Ω_x, normal curvature Ω_y and geodesic curvature Ω_z, which are the angular rate of the Darboux frame, expressed along the axes of the Darboux frame itself. The resulting relationships are obtained from the well known Frenet-Serret formula

$$\theta' = \kappa \frac{\cos(\nu - \phi)}{\cos\mu} = \frac{\Omega_y \sin\phi + \Omega_z \cos\phi}{\cos\mu}, \tag{1}$$

$$\mu' = \kappa \sin(\nu - \phi) = \Omega_y \cos\phi - \Omega_z \sin\phi, \tag{2}$$

$$\phi' = \tau + \nu' + \kappa \tan\mu \cos(\nu - \phi) = \Omega_x + \tan\mu(\Omega_y \sin\phi + \Omega_z \cos\phi), \tag{3}$$

where the prime means derivative with respect to s. The position $[x, y, z]^T$ of the origin of the Darboux frame, expressed in the absolute ground frame, is obtained from

$$\begin{bmatrix} x \\ y \\ z \end{bmatrix} = \int \boldsymbol{t} ds = \int \begin{bmatrix} \cos\theta\cos\mu \\ \sin\theta\cos\mu \\ -\sin\mu \end{bmatrix} ds, \tag{4}$$

where $\boldsymbol{t}$ is the tangent to the road centreline, which is the first column of the rotation matrix associated to the Darboux frame.

Once the road is defined, the vehicle position can be given in terms of the lateral distance n from the road centreline and relative orientation χ with respect to the tangent to the road centreline. Such quantities can be either related to the longitudinal u and lateral v velocities of a vehicle reference point (expressed in its own reference frame and assumed to lie on the road plane) or to the total velocity $V = \sqrt{u^2 + v^2}$ and drift angle $\beta = \arctan(v/u)$ of the vehicle reference point

$$n' = \frac{1}{\dot{s}}(u \sin\chi + v \cos\chi) = \frac{1}{\dot{s}} V \sin(\chi + \beta), \tag{5}$$

$$\chi' = \frac{1}{\dot{s}}(\omega_z - \Omega_z \dot{s}) = \frac{1}{\dot{s}}(\hat{\omega}_z - \Omega_z \dot{s} - \dot{\beta}), \tag{6}$$

where ω_z is the angular velocity of vehicle frame attached to the reference point (aligned with the vehicle longitudinal axis), while $\hat{\omega}_z$ is the angular velocity of the vehicle frame attached to the reference point and aligned with the total velocity and the trajectory – and $\dot{s}$ is the speed of travelling along the centreline, which is given by

$$\dot{s} = \frac{u \cos\chi - v \sin\chi}{1 - n\Omega_z} = \frac{V \cos(\chi + \beta)}{1 - n\Omega_z}. \tag{7}$$

All equations have been given as a function of the travelled distance instead of time. Indeed, it is common to solve minimum time problem in the space domain. The link between the space- and time-domain formulations is (7), since $d\boldsymbol{x}/dt = \dot{s}\, d\boldsymbol{x}/ds$. The angular velocities of the vehicle reference point are computed from to road curvatures and travelling speed $\dot{s}$ using

$$\omega_x = (\Omega_x \cos\chi + \Omega_y \sin\chi)\dot{s}, \tag{8}$$

$$\omega_y = (\Omega_y \cos\chi - \Omega_x \sin\chi)\dot{s}, \tag{9}$$

together with (6). Under the common assumption that the road curvatures Ω_x and Ω_y are small, the longitudinal and lateral accelerations of the vehicle reference point expressed in the vehicle frame (i.e. rotated by χ with respect to the centreline tangent) a_x, a_y, or expressed in a frame aligned with the total velocity, i.e. with the trajectory of the vehicle reference point (rotated by $\chi + \beta$ with respect to the centreline tangent), $\hat{a}_x, \hat{a}_y$, are given by (see Fig. 1)

$$a_x = \dot{u} - v(\dot{\chi} + \Omega_z \dot{s}), \qquad \hat{a}_x = \dot{V}, \tag{10}$$

$$a_y = \dot{v} + u(\dot{\chi} + \Omega_z \dot{s}), \qquad \hat{a}_y = V(\dot{\chi} + \Omega_z \dot{s} + \dot{\beta}), \tag{11}$$

where the hat denotes variables related to the frame aligned with the vehicle trajectory, while $\dot{\beta} = 0$ in the case of quasi-steady-state conditions. It is worth noting that $\omega_z = \dot{\chi} + \Omega_z \dot{s}$ and $\hat{\omega}_z = \dot{\chi} + \Omega_z \dot{s} + \dot{\beta}$.

3. g-g-g diagrams

The standard g-g diagrams give information related to the vehicle performance on a two-dimensional track. They can be extended to deal with three-dimensional scenarios, and in particular to include the effect of road banking, road slope and the related rate of change. The quasi-steady-state equations and g-g-g diagrams of a motorcycle and a car are derived in the following two subsections. The inspection of terms suggests the best parametrization of the maps for the subsequent minimum-time OCP problem.

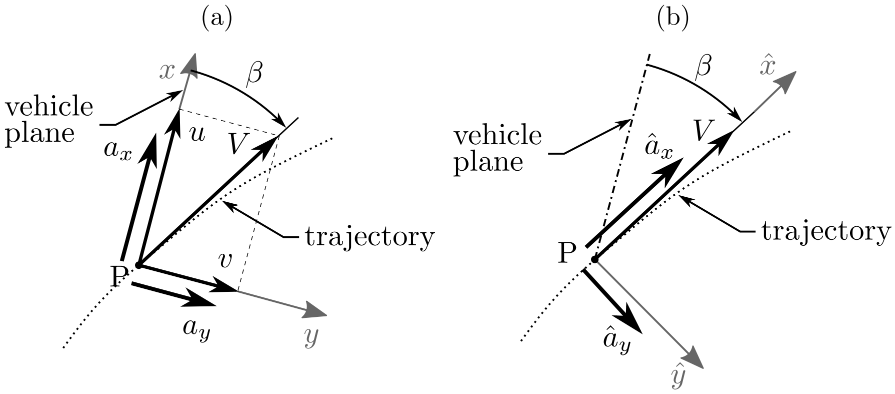

Figure 1.: Lateral and longitudinal accelerations of the vehicle reference point P: (a) expressed in the vehicle reference frame, and (b) expressed in a frame aligned with the total velocity V (i.e. tangent to the trajectory).

3.1. *Motorcycle model*

The quasi-steady-state equations of a motorcycle on a three-dimensional track are obtained by a generalization of the equations reported in [30]. The assumptions remain the same, namely both the suspensions and the steer angle are neglected, the vehicle is assumed symmetric with respect to the x-z plane (i.e. $I_{xy} = I_{yz} = 0$), the cross moment of inertia I_{xz} is assumed negligible and $I_y = I_z$; see Fig. 2. The following equations of motion are obtained

$$m\tilde{a}_x = F_{xr} + F_{xf} - F_D, \tag{12}$$

$$m\tilde{a}_y = F_{yr} + F_{yf}, \tag{13}$$

$$m\tilde{g} = N_r + N_f, \tag{14}$$

$$m\tilde{a}_y h\cos\tilde{\varphi} = m\tilde{g}h\sin\tilde{\varphi}, \tag{15}$$

$$m\tilde{a}_x h\cos\tilde{\varphi} = bN_r - (w-b)N_f - F_D h_a\cos\tilde{\varphi}, \tag{16}$$

$$m\tilde{a}_x h\sin\tilde{\varphi} = bF_{yr} - (w-b)F_{yf} - F_D h_a\sin\tilde{\varphi}, \tag{17}$$

where

$$\tilde{a}_x = a_x + g\sin\mu, \tag{18}$$

$$\tilde{a}_y = a_y - g\cos\mu\sin\phi, \tag{19}$$

$$\tilde{g} = g\cos\mu\cos\phi + \omega_y V, \tag{20}$$

with V the velocity of the centre of mass, a_x and a_y the longitudinal and lateral accelerations expressed in the vehicle reference frame on the road plane, which has slope μ (positive when going uphill) and banking ϕ (positive in the direction of the positive roll), ω_y is the angular velocity along the y-axis, and g the gravity (along the ground vertical axis). The tilde denotes variables which define the accelerations used to parametrize the g-g-g maps. It is worth noting that $\tilde{a}_x, \tilde{a}_y, \tilde{g}$ are the accelerations possibly measured by an inertial measurement unit mounted on the bike, after projection on the road plane.

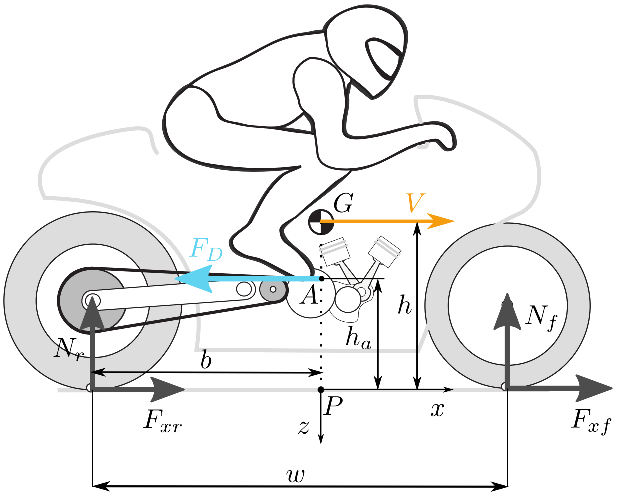

Figure 2.: Motorcycle model.

From (15) one obtains the camber angle

$$\tilde{\varphi} = \arctan \frac{\tilde{a}_y}{\tilde{g}}, \tag{21}$$

from which the roll angle is obtained as $\varphi = \tilde{\varphi} + \phi$. It is worth noting that (12)-(15) are identical to those reported in [30], when the accelerations are taken from (18)-(20). As a consequence, also the accelerations limits, and the related derivations, are identical, once accelerations (18)-(20) are introduced.

The acceleration limit related to the tyre friction is

$$\left(\frac{w(m\tilde{a}_x + F_D)\sqrt{\tilde{a}_y^2 + \tilde{g}^2}}{g((w-b)m\sqrt{\tilde{a}_y^2 + \tilde{g}^2} + m\tilde{a}_x h + F_D h_a)} \right)^2 \frac{1}{\mu_x^2} + \left(\frac{\tilde{a}_y}{\tilde{g}} \right)^2 \frac{1}{\mu_y^2} = 1, \tag{22}$$

while the deceleration limit related to the tyre friction is

$$-\tilde{a}_x = \tilde{g}\mu_x \sqrt{1 - \left(\frac{\tilde{a}_y}{\tilde{g}} \right)^2 \frac{1}{\mu_y^2}} + \frac{F_D}{m}, \tag{23}$$

and it is attained with the following (optimal) brake ratio

$$\gamma_{opt} = \left. \frac{F_{xf}}{F_{xr}} \right|_{opt} = \frac{mb\sqrt{\tilde{a}_y^2 + \tilde{g}^2} - m\tilde{a}_x h - F_D h_a}{m(w-b)\sqrt{\tilde{a}_y^2 + \tilde{g}^2} + m\tilde{a}_x h + F_D h_a}. \tag{24}$$

The maximum acceleration is further limited by the engine power $P_{\max}$

$$\tilde{a}_x = \frac{P_{\max}}{mV} - \frac{F_D}{m}, \tag{25}$$

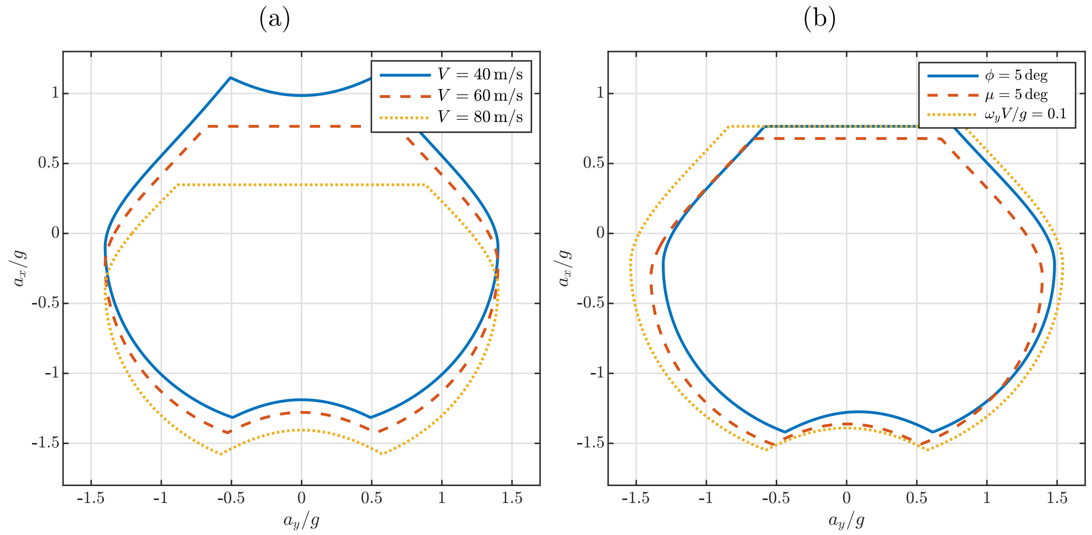

Figure 3.: Motorcycle g-g diagrams: (a) at different speeds V and (b) with banking ϕ, slope μ and slope rate ω_y at $V = 60\,\mathrm{m/s}$.

and the wheelie limit (i.e. when the front tyre lifts from the road)

$$\tilde{a}_x = \frac{b\sqrt{\tilde{a}_y^2 + \tilde{g}^2}}{h} - \frac{F_D h_a}{mh}. \tag{26}$$

Finally, the maximum deceleration is limited by the stoppie (the rear tyre lifts from the road)

$$-\tilde{a}_x = \frac{(w-b)\sqrt{\tilde{a}_y^2 + \tilde{g}^2}}{h} + \frac{F_D h_a}{mh}. \tag{27}$$

In sum, the g-g-g diagram is obtained by the envelope of (22), (23), (25), (26), and (27). For example, one can assume the velocity V, the accelerations $\tilde{a}_y, \tilde{g}$ and then solve for $\tilde{a}_x$. From these accelerations $\tilde{a}_x, \tilde{a}_y, \tilde{g}$, one can compute the accelerations projected on the road plane a_x, a_y through (18)-(20), given the road banking, the road slope and slope rate.

Some sections of the g-g-g of the motorcycle with the dataset in Tab. 1 are given in Fig. 3. Fig. 3a shows that at low speeds both wheelie and stoppie limits are visible, while at high speeds there is no wheelie limit because the maximum acceleration is limited by the engine power. In Fig. 3b the effect of road banking, slope and slope rate is shown: the banking ϕ makes the g-g diagram asymmetric with respect to the vertical axis $a_y = 0$ (higher lateral acceleration are possible when turning on the direction of banking, while they reduce in adverse banking conditions), the slope μ shifts the g-g diagram vertically (lower accelerations are possible when going uphill and larger accelerations when going downhill), while the slope rate ω_y changes the size of the g-g diagram (higher accelerations are possible when going through to the bottom of a valley – positive ω_y – while smaller accelerations are possible when going over the brow of a hill).

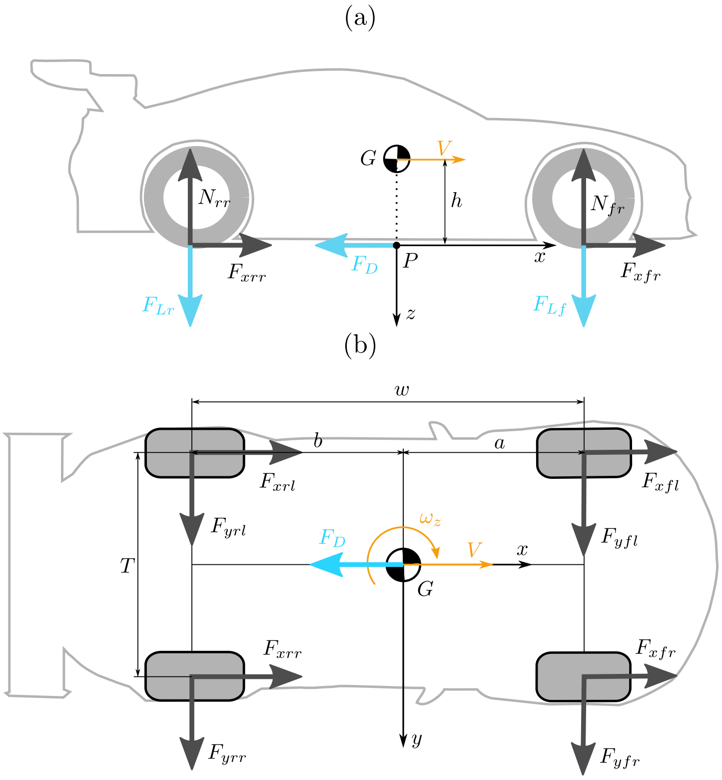

Figure 4.: Car model: side view (a) and top view (b).

3.2. *Car model*

The quasi-steady-state equations of a car on a three-dimensional track are obtained by a generalization of the equations reported in [30]. The assumptions remain the same, namely that the wheel-steering angle δ is assumed small, the roll, pitch and bounce degrees of freedom are neglected, together with the suspension travels; Fig. 4. The following equations are obtained, once $I_y = I_z$ and $I_{xz} = 0$ are assumed (as in Sec. 3.1)

$$
\begin{aligned}
m\tilde{a}_x &= (F_{xfl} + F_{xfr} + F_{xrl} + F_{xrr}) - (F_{yfl} + F_{yfr})\,\delta - F_D, && (28)\\
m\tilde{a}_y &= (F_{yfl} + F_{yfr} + F_{yrl} + F_{yrr}) + (F_{xfl} + F_{xfr})\,\delta, && (29)\\
m\tilde{g} &= (N_{fl} + N_{fr} + N_{rl} + N_{rr}) - (F_{Lf} + F_{Lr}), && (30)\\
m\tilde{a}_y h &= \frac{T}{2}(N_{fl} - N_{fr} + N_{rl} - N_{rr}), && (31)\\
m\tilde{a}_x\, h &= -a(N_{fl} + N_{fr}) + b(N_{rl} + N_{rr}) + aF_{Lf} - bF_{Lr}, && (32)\\
0 &= -\frac{T}{2}\,(F_{yfl} - F_{yfr})\,\delta + a\,(F_{xfl} + F_{xfr})\,\delta + \frac{T}{2}\,(F_{xfl} - F_{xfr} + F_{xrl} - F_{xrr}) + \\
&\quad + a\,(F_{yfl} + F_{yfr}) - b\,(F_{yrl} + F_{yrr})\,, && (33)
\end{aligned}
$$

where again the accelerations $\tilde{a}_x, \tilde{a}_y, \tilde{g}$ are given by (18)-(20). The equations are identical to those presented in [30], once a_x, a_y, g are replaced by $\tilde{a}_x, \tilde{a}_y, \tilde{g}$.

The total driving force F_x is split between the rear and front axle according to the distribution factor k_t, under the open-differential assumption

$$F_{xfl} = \frac{(1-k_t)F_x}{2}, \qquad F_{xfr} = \frac{(1-k_t)F_x}{2}, \tag{34}$$

$$F_{xrl} = \frac{k_t F_x}{2}, \qquad F_{xrr} = \frac{k_t F_x}{2}. \tag{35}$$

In acceleration $k_t = 1$ for rear-wheel-drive (RWD) vehicles, $k_t = 0$ for front-wheel-drive (FWD) vehicles, and $0 < k_t < 1$ for all-wheel-drive (AWD) vehicles. In braking

$$k_t = \frac{1}{1+\gamma}, \qquad \gamma = \frac{F_{xfl} + F_{xfr}}{F_{xrl} + F_{xrr}}, \tag{36}$$

where γ is the brake ratio, which is here defined as the ratio between the front and rear longitudinal tyre forces. A standard roll stiffness balance equation is included to solve the lateral load transfer from the roll stiffness ratio ξ

$$\xi = \frac{N_{fl} - N_{fr}}{(N_{fl} - N_{fr}) + (N_{rl} - N_{rr})}. \tag{37}$$

In order to obtain the g-g-g maps of the car semi-analytically, the steer angle is neglected, as in the case of the motorcycle in Sec. 3.1. In addition, the following relationships between lateral and normal forces are included

$$\frac{F_{yfl}}{N_{fl}} = \frac{F_{yfr}}{N_{fr}}, \qquad \frac{F_{yrl}}{N_{rl}} = \frac{F_{yrr}}{N_{rr}}. \tag{38}$$

In practice, enforcing (38) means including the main assumption of the standard single-track car model in the double-track model (same cornering stiffness and slip on the tyres of the same axle). Yet the double-track model retains the lateral load transfer, which will in turn affect significantly the limit lateral accelerations.

In sum, there are 13 quasi-steady-state equations, namely (28)-(35),(37),(38) that can be solved for 13 unknowns, namely the force F_x, the four tyre normal loads $(N_{fl}, N_{fr}, N_{rl}, N_{rr})$, the four tyre lateral forces $(F_{yfl}, F_{yfr}, F_{yrl}, F_{yrr})$, and the four longitudinal forces $(F_{xfl}, F_{xfr}, F_{xrl}, F_{xrr})$, once the velocity V and accelerations $\tilde{a}_x, \tilde{a}_y, \tilde{g}$, together with the distribution factor k_t are given. Alternatively, as in the case of the motorcycle, one can give the velocity V of the centre of mass and the accelerations in the road plane a_x, a_y, which combine with the road banking ϕ, slope μ and angular velocity ω_y to give $\tilde{a}_x, \tilde{a}_y, \tilde{g}$. The g-g-g diagram is obtained by introducing the quasi-steady-state solution into the tyre friction ellipses

$$\left(\frac{F_{xfl}/N_{fl}}{\mu_{x,fl}}\right)^2 + \left(\frac{F_{yfl}/N_{fl}}{\mu_{y,fl}}\right)^2 \leq 1 \qquad \left(\frac{F_{xfr}/N_{fr}}{\mu_{x,fr}}\right)^2 + \left(\frac{F_{yfr}/N_{fr}}{\mu_{y,fr}}\right)^2 \leq 1 \tag{39}$$

$$\left(\frac{F_{xrl}/N_{rl}}{\mu_{x,rl}}\right)^2 + \left(\frac{F_{yrl}/N_{rl}}{\mu_{y,rl}}\right)^2 \leq 1 \qquad \left(\frac{F_{xrr}/N_{rr}}{\mu_{x,rr}}\right)^2 + \left(\frac{F_{yrr}/N_{rr}}{\mu_{y,rr}}\right)^2 \leq 1 \tag{40}$$

The following expressions are obtained

$$\left[\frac{\frac{1}{2}(1-k_t)(m\tilde{a}_x+F_D)}{\frac{1}{2}m\tilde{g}\frac{b}{a+b}+\frac{1}{2}F_{Lf}-\frac{1}{2}m\tilde{a}_x\frac{h}{a+b}+m\tilde{a}_y\frac{h}{T}\xi}\right]^2\frac{1}{\mu_{x,fl}^2}+\left(\frac{\frac{b}{a+b}m\tilde{a}_y}{\frac{b}{a+b}m\tilde{g}-m\tilde{a}_x\frac{h}{a+b}+F_{Lf}}\right)^2\frac{1}{\mu_{y,fl}^2}=1 \tag{41}$$

$$\left[\frac{\frac{1}{2}(1-k_t)(m\tilde{a}_x+F_D)}{\frac{1}{2}m\tilde{g}\frac{b}{a+b}+\frac{1}{2}F_{Lf}-\frac{1}{2}m\tilde{a}_x\frac{h}{a+b}-m\tilde{a}_y\frac{h}{T}\xi}\right]^2\frac{1}{\mu_{x,fr}^2}+\left(\frac{\frac{b}{a+b}m\tilde{a}_y}{\frac{b}{a+b}m\tilde{g}-m\tilde{a}_x\frac{h}{a+b}+F_{Lf}}\right)^2\frac{1}{\mu_{y,fr}^2}=1 \tag{42}$$

$$\left[\frac{\frac{1}{2}k_t(m\tilde{a}_x+F_D)}{\frac{1}{2}m\tilde{g}\frac{a}{a+b}+\frac{1}{2}F_{Lr}+\frac{1}{2}m\tilde{a}_x\frac{h}{a+b}+m\tilde{a}_y\frac{h}{T}(1-\xi)}\right]^2\frac{1}{\mu_{x,rl}^2}+\left(\frac{\frac{a}{a+b}m\tilde{a}_y}{\frac{a}{a+b}m\tilde{g}+m\tilde{a}_x\frac{h}{a+b}+F_{Lr}}\right)^2\frac{1}{\mu_{y,rl}^2}=1 \tag{43}$$

$$\left[\frac{\frac{1}{2}k_t(m\tilde{a}_x+F_D)}{\frac{1}{2}m\tilde{g}\frac{a}{a+b}+\frac{1}{2}F_{Lr}+\frac{1}{2}m\tilde{a}_x\frac{h}{a+b}-m\tilde{a}_y\frac{h}{T}(1-\xi)}\right]^2\frac{1}{\mu_{x,rr}^2}+\left(\frac{\frac{a}{a+b}m\tilde{a}_y}{\frac{a}{a+b}m\tilde{g}+m\tilde{a}_x\frac{h}{a+b}+F_{Lr}}\right)^2\frac{1}{\mu_{y,rr}^2}=1 \tag{44}$$

which can be solved for $\tilde{a}_x$ given $\tilde{a}_y$, or viceversa – the limit accelerations is the minimum value obtained from (41)-(44). The friction coefficients $\mu_{x,ij}$, $\mu_{y,ij}$ (where $i=f,r$ and $j=l,r$) are assumed load-dependent, which does not add much complexity to the model and allow to obtain realistic maps – without such effects the maximum lateral accelerations are excessive and the shape of the g-g around them is too sharp, when compared to the real-world behaviour. Following the approach in [32], the friction coefficients are given by

$$\mu_{x,ij}=p_{Dx1}+p_{Dx2}df_{z,ij}, \tag{45}$$

$$\mu_{x,ij}=p_{Dy1}+p_{Dy2}df_{z,ij}, \tag{46}$$

where $df_{z,ij}=(N_{ij}-N_0)/N_0$ and N_0 is a reference load of the tyre. The aerodynamics forces consist of the drag force F_D, the front F_{Lf} and rear F_{Lr} downforces. They are applied on the road plane (see Fig. 4a), and are given by

$$F_D=\frac{1}{2}\rho_a C_D A V^2, \qquad F_{Lf}=\frac{1}{2}\rho_a C_{Lf} A V^2, \qquad F_{Lr}=\frac{1}{2}\rho_a C_{Lr} A V^2. \tag{47}$$

The g-g-g map is obtained from the envelope of (41)-(44), together with the engine power limit, which has the same expression employed with the motorcycle model, i.e. (25).

Some sections of the g-g-g of the car with the dataset in Tab. 2 are given in Fig. 5. In Fig. 5a the effect of speed is shown: at low speeds the accelerations are limited by the tyre friction ellipses, while at high speeds they are limited by the engine power. It is also visible the very large contribution of aerodynamics: as the speed increases, the g-g diagram enlarges, i.e. larger lateral accelerations are possible as well as larger decelerations (e.g. lateral acceleration up to 4.5 g and deceleration up to 6 g at 80 m/s are achievable, even if the tyre-road friction coefficients do not exceed 1.7 in the related loading condition) – this is a well known behaviour for formula cars. In Fig. 5b the effect of road banking, slope and slope rate is shown. The behaviour is similar to the one discussed for the motorcycle, i.e. the road baking makes the g-g asymmetric, the slope shifts the g-g in the vertical direction, while the slope rate changes the size of the g-g. In the formula car considered, the effect of three-dimensionality is smaller when compared with the effect of aerodynamics. However, the absolute values are similar to those observed on the motorcycle.

3.3. *Parametrization*

The inspection of the quasi-steady-state equations suggests that the g-g-g diagram can be parametrized in terms of the three accelerations $\tilde{a}_x, \tilde{a}_y, \tilde{g}$ and the velocity V. Similarly to [30], polar coordinates are conveniently employed. Remaining within the g-g-g boundaries means enforcing the following constraint

$$\tilde{\rho} \leq \tilde{\rho}_{\text{max}}(\tilde{\alpha}, V, \tilde{g}) \tag{48}$$

where $\tilde{\rho}$ is the engaged friction radius given by

$$\tilde{\rho} = \frac{1}{g}\sqrt{\tilde{a}_x^2 + \tilde{a}_y^2}, \tag{49}$$

and $\tilde{\rho}_{\text{max}}$ is the maximum friction radius (boundary of the g-g-g). The orientation of the engaged friction radius is given by

$$\tilde{\alpha} = \arctan 2\left(\tilde{a}_x, \tilde{a}_y\right). \tag{50}$$

The values of the adherence radius in different conditions are interpolated by means of multivariate modified Akima interpolation, to give a 4-dimensional $\mathcal{C}^1$ (i.e. continuously differentiable) surface. The modified Akima algorithm, instead of other popular splines such as the standard cubic splines, allows to obtain a smoother surface, while avoiding undulations between the grid points. Moreover, the $\mathcal{C}^1$-periodicity along $\tilde{\alpha}$ is enforced so as to ensure a smooth transition from $\tilde{\alpha} = \pi$ to $\tilde{\alpha} = -\pi$ and viceversa.

As a final remark, it is worth noting that the g-g-g diagrams should be expressed in a reference frame aligned with the total velocity $V = \sqrt{u^2 + v^2}$, which is tangent to

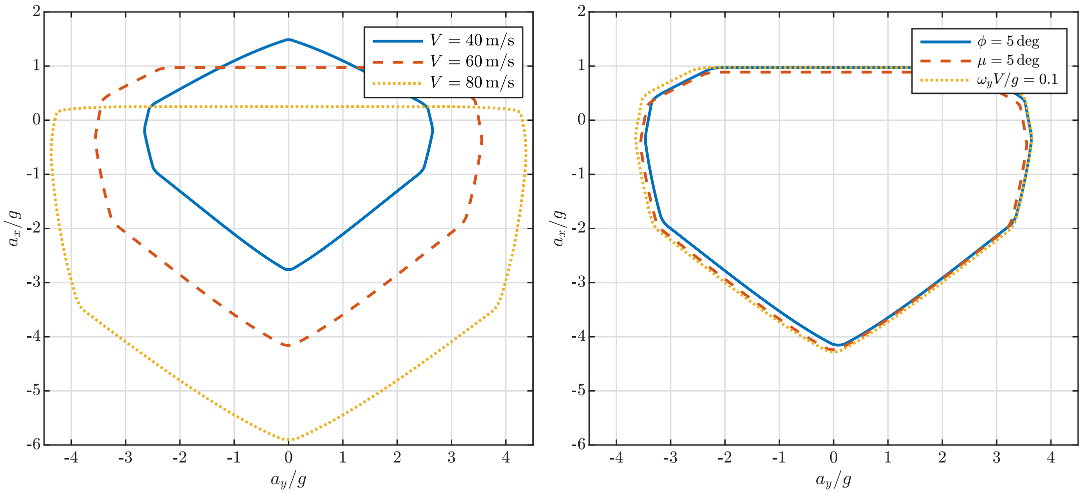
(a) (b)

Figure 5.: Car g-g diagrams: (a) at different speeds V and (b) with banking ϕ, slope μ and slope rate ω_y at $V = 60\,\mathrm{m/s}$.

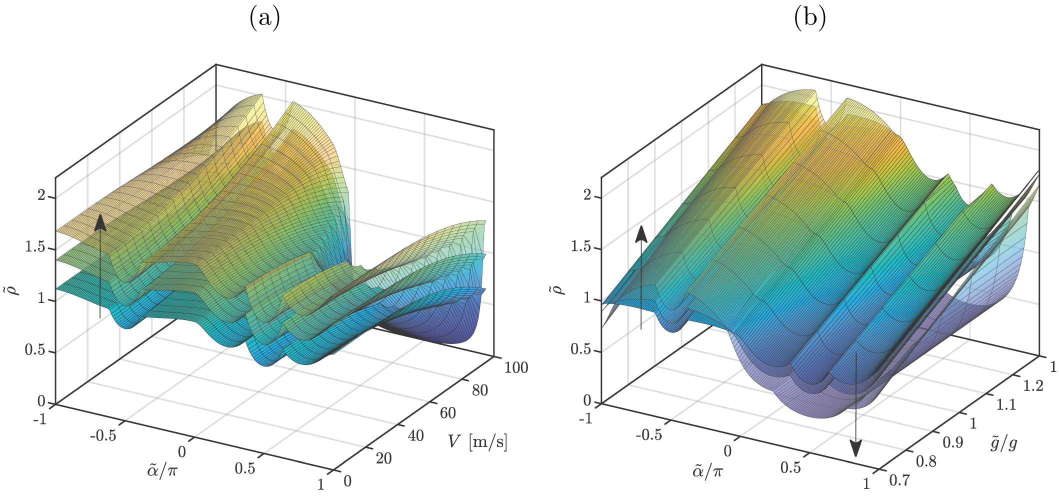

Figure 6.: Motorcycle adherence radius hyper-surfaces: (a) iso-$\tilde{g}$ with $\tilde{g} = (0.8, 1.0, 1.2)g$ and (b) iso-V with $V = (40, 60, 80)$ m/s; the arrows indicate the direction of variation when increasing the iso-parameter.

the vehicle trajectory. Many times such diagrams are instead computed in a reference aligned with the vehicle axes. In these scenarios, the calculated maps need be rotated by the vehicle slip angle $\beta = \arctan(\frac{v}{u})$, before being used with the method presented in this paper.

4. Free-trajectory OCP

The problem consists in minimizing the manoeuvre time of a three-degrees-of-freedom model, which is constrained to remain within the track borders and within the limits of the g-g-g diagrams. All the complexity of the model is confined within the g-g-g diagram, which can be either derived from a numerical model (for example, but not necessarily, one of those reported in Sec. 3.1 and Sec. 3.2) or from experiments.

The state variables vector $\mathbf{x}$ of the OCP consists of the velocity V of the vehicle reference point along the trajectory, the lateral position n of such reference point with respect to the road centreline, and the relative orientation $\hat{\chi}$ of V with respect to the tangent to the centreline (see Fig. 7)

$$\mathbf{x} = [V,\, n,\, \hat{\chi}]^T. \tag{51}$$

It is worth noting that $\hat{\chi} = \chi + \beta$. The control vector $\mathbf{u}$ of the OCP consists of the acceleration $\hat{a}_x$ along the trajectory and acceleration $\hat{a}_y$ normal to the trajectory

$$\mathbf{u} = [\hat{a}_x, \hat{a}_y]^T. \tag{52}$$

The differential equations of the OCP, already expressed in the space domain using

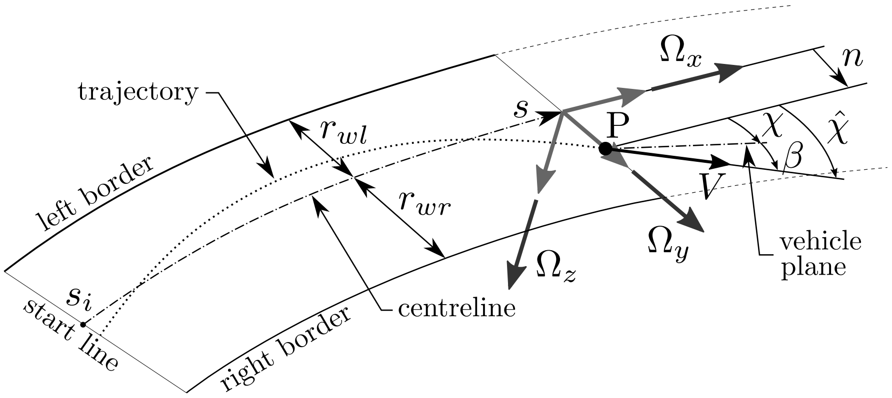

Figure 7.: Three-dimensional road modelling with relative torsion Ω_x, normal curvature Ω_y and geodesic curvature Ω_z, and vehicle positioning with lateral position n of the vehicle reference point P and relative angle $\hat{\chi}$ of the total velocity V with respect to the centreline on the road tangent plane.

$d\boldsymbol{x}/dt = \dot{s}\, d\boldsymbol{x}/ds$, are given by

$$V' = \frac{\hat{a}_x}{\dot{s}}, \tag{53}$$

$$n' = \frac{V}{\dot{s}} \sin\hat{\chi}, \tag{54}$$

$$\hat{\chi}' = \frac{1}{\dot{s}} \frac{\hat{a}_y}{V} - \Omega_z, \tag{55}$$

where $\dot{s}$ is computed using (7), while (54) and (55) are obtained from (5) and (6) with (11). In order to obtain smoother solutions, the derivatives of the accelerations (i.e. the jerks) may be controlled instead of the accelerations: in this case the input vector becomes $\boldsymbol{u} = [\hat{j}_x, \hat{j}_y]^T$ and two more equations need be added, namely $\hat{a}'_x = \hat{j}_x/\dot{s}$ and $\hat{a}'_y = \hat{j}_y/\dot{s}$.

The target $\mathcal{L}$ of the OCP is the manoeuvre time

$$\mathcal{L} = \int_{s_i}^{s_e} \frac{1}{\dot{s}}\, ds, \tag{56}$$

where $s_e - s_i$ represent the track length. It is often convenient to add some regularization terms in the integrand of (56) to avoid numerical issues such as singularities [29]. Cyclic conditions are enforced in the case of lap-time simulations, i.e. the states at the beginning and end of the lap, i.e. on the start/finish line, are identical

$$\boldsymbol{x}(s_i) = \boldsymbol{x}(s_e). \tag{57}$$

The vehicle is constrained to move within the road borders

$$-r_{wl} + T/2 \leq n \leq r_{wr} - T/2, \tag{58}$$

where r_{wl} and r_{wr} represent the left and right road widths and T is the vehicle track width – clearly it is $T = 0$ in the case of motorcycles. The constraint related to the g-g-g envelope is given by

$$\tilde{\rho} \leq \tilde{\rho}_{\max},$$

with $\tilde{\rho}$ and $\tilde{\rho}_{\max}$ from (49) and (48).

In sum, the OCP controls the accelerations along the trajectory $\hat{a}_x, \hat{a}_y$, from which the corresponding $\tilde{a}_x, \tilde{a}_y, \tilde{g}$ are derived and used to ensure that the g-g-g envelope constraint is enforced. The OCP results consist of the optimal trajectory, expressed in the curvilinear coordinates $[s, n, \hat{\chi}]^T$, and the speed profile V. The full vehicle states can be retrieved from the quasi-steady-state solution of the model used to generate the g-g-g maps. Indeed, each point of the OCP solution is associated to a point in the g-g-g diagram, and thus to the states of the corresponding quasi-steady-state solution. The resulting OCP can then be solved numerically using direct or indirect methods [28].

5. Examples of application

The OCP illustrated in Sec. 4 is now employed with the g-g-g diagrams derived from the motorcycle and car models in Sec. 3, on two three-dimensional tracks described with the approach in Sec. 2. The Mugello (Italy) and Barcelona-Catalunya (Spain) tracks are selected, because their geometries can be retrieved from the literature, e.g. from [26, 27] and [31], respectively. Datasets for a racing motorcycle and a racing car are employed. The motorcycle dataset resembles those used in [26, 27], while the car dataset resembles that of the formula one in [31].

The procedure for both the car and the motorcycle is the same. First, the g-g-g diagrams for each vehicle are obtained: the speed V is varied from 0 to 90 m/s by steps of 5 m/s, the orientation $\tilde{\alpha}$ of the adherence radius is varied by steps of 1 deg, the ac-

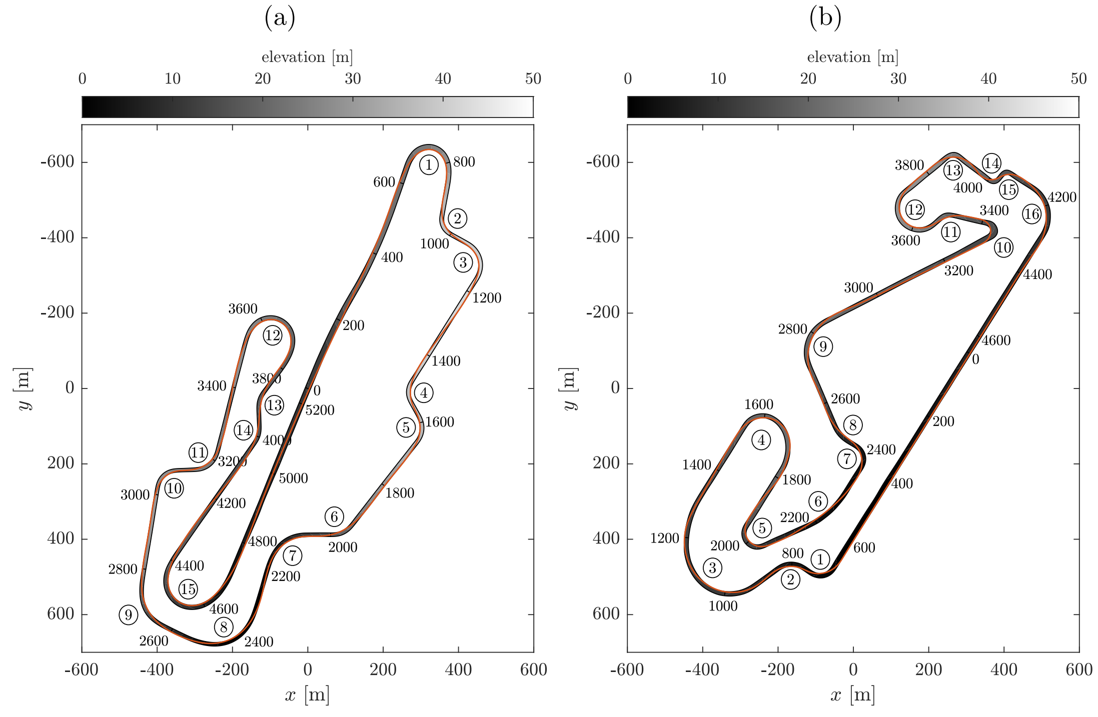

Figure 8.: Optimal 3D trajectories: (a) motorcycle on Mugello and (b) car on Catalunya.

celeration $\tilde{g}/g$ is varied from 0.6 to 1.4 by steps of 0.1. Second, all g-g-g diagrams (for each vehicle) are combined to give the adherence radius hyper-surface. Third, each adherence radius hyper-surface is interpolated by means of the modified Akima piecewise cubic Hermite interpolation. Fourth, the OCP problem is run on the selected tracks. The direct solution method in [28, 33] is employed to solve the OCP, in combination with the NLP solver IPOPT [34].

5.1. *Motorcycle*

Fig. 8a shows the optimal trajectory on the Mugello circuit for the motorcycle considered in this work, while Fig. 9a and Fig. 10a show the lateral position (with respect to the centreline) and velocity on the Mugello and Catalunya circuits. The simulated lap times on the two circuits are 105.313 s and 105.952 s, while the top speeds are 333 km/h and 327 km/h, respectively. The speeds in the Arrabbiata 2 and Bucine (turn 9 and 15 of the Mugello circuit) are 162 km/h and 111 km/h, respectively. The motorcycle results in the Mugello circuit are in line with those reported in [26, 27], which employed dynamic motorcycle models (i.e. not quasi-steady-state), the former solved with a direct method and the latter with an indirect method. In addition, also the effect of three-dimensionality is quantitatively similar. Indeed, the lap time increases by 4.0 s when running on a 'flat' Mugello, which is again in line with the results in [26, 27] – the speed difference (two- vs. three-dimensional track) are especially relevant around turn 8 and 9 (Arrabbiata 1 and Arrabbiata 2), while the lateral position difference (two- vs. three-dimensional track) are especially relevant between turn 7 and 8 (Savelli and Arrabbiata 1); see Fig. 9a. On the contrary, the effect of three-dimensionality is reversed and much less significant in the Catalunya circuit. The simulation on the 'flat' Catalunya is 0.7 s faster than the one on the three-dimensional track – the speed and trajectories are closer to one-another when comparing the results on the two- and three-dimensional tracks. Finally, it is also worth noting that the geometry of the Catalunya is the same for both the motorcycle and the car simulations, and corresponds to the one in [31]. Therefore, modifications carried out afterwards are not included.

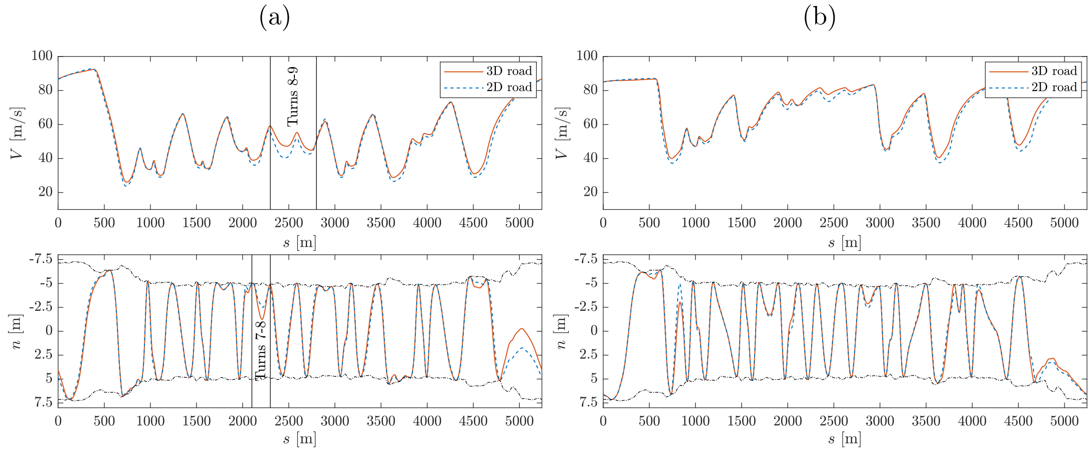
(a) (b)

Figure 9.: Effect of three-dimensionality on the velocity V (top) and lateral position n (bottom) on Mugello for the motorcycle (a) and the car (b) – the dot-dashed line represents the road width.

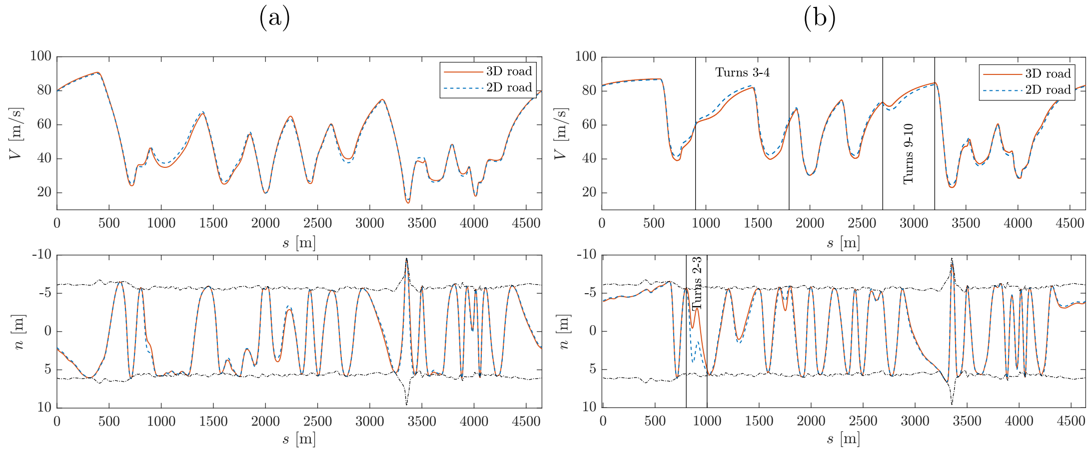

Figure 10.: Effect of three-dimensionality on the velocity V (top) and lateral position n (bottom) on Catalunya for the motorcycle (a) and the car (b) – the dot-dashed line represents the road width.

5.2. *Car*

Fig. 8b shows the optimal trajectory on the Catalunya circuit for the car considered in this work, while Fig. 9b and Fig. 10b show the lateral position (with respect to the centreline) and velocity on Mugello and Catalunya. The simulated lap times on the two circuits are 77.274 s and 81.031 s, while the top speeds are 312 km/h and 314 km/h, respectively. The speeds in turn 1 and 5 of the Catalunya circuit are 141 km/h and 109 km/h, respectively. The car results in the Catalunya circuit are in line with those reported in [31], which employed a dynamic car model. In addition, also the effect of three-dimensionality is quantitatively similar. Indeed, the lap time reduces by 0.9 s when running on a 'flat' Catalunya, which is again in line with the results in [31] – the speed difference (two- vs. three-dimensional track) are visible between turn 3 and 4 (three-dimensional solution is slower) and between turn 9 and 10 (the three-dimensional solution is faster), while the lateral position difference (two- vs. three-dimensional track) is visible between turn 2 and 3. On the contrary, the effect of three-dimensionality is reversed and much more significant in the Mugello. The simulation on the 'flat' Mugello is 2.7 s slower than the one on the three-dimensional track – as in the case of the motorcycle, the Mugello proves to be a circuit where the effects of three-dimensionality are quite relevant.

5.3. *Remarks on problem size*

The computational effort of the method proposed can be assessed in terms of the number of equations (state equations plus constraints) that need be solved and the related CPU time. All the results reported in this work have been started with a coarse mesh, consisting of 41 equally spaced mesh points (i.e. one point every 128 m in the Mugello and one point every 113 m in the Catalunya circuit), resulting in 327 equations (per circuit). The error for the IPOPT solver is 10^{-7}, while the tolerance for the mesh refinement in GPOPS-II is 2×10^{-4}; all variables are scaled based on a reference length, a reference mass and a reference time [29]. Numerical differentiation is employed. After 5 mesh-refinements, which is the number of refinements required to solve the problem, the free-trajectory OCPs consist of a number of equations between 11 231 and 12 975 (depending on the vehicle/circuit combination), when the jerks $\hat{j}_x$ and $\hat{j}_y$ are used as controls. The corresponding maximum and minimum mesh spacing is 14 m and 0.33 m in the Mugello, while it is 24 m and 0.21 m in the Catalunya circuit. The CPU times range from 74 s to 272 s, depending on the vehicle/circuit combination.

In the case the accelerations $\hat{a}_x$ and $\hat{a}_y$ are directly controlled (instead of the jerks), the number of equations of the free-trajectory OCPs reduces to 8 735–9 935 (depending on the vehicle/track combination), after 6 mesh-refinements, which are required to solve the problem. The maximum and minimum mesh spacing is 14 m and 0.28 m in the Mugello, while it is 18 m and 0.21 m in the Catalunya circuit, and the CPU times increase to 220–624 s, depending on the vehicle/circuit combination. In general, the solution obtained when controlling directly the accelerations is sharper (in the accelerations) and more difficult to converge, when compared against the one obtained controlling the jerks.

In sum, controlling the jerks makes the solution faster, although with a larger number of equations. The solution time of the proposed approach remains significantly smaller than the typical solution time experienced with the full dynamic models – at least by a factor 10 in the implementations by the authors. The time to compute the g-g-g-V maps is not included – indeed the maps remain the same when changing the track.

5.4. *Remarks on fixed-trajectory*

Similarly to [30], also the free-trajectory method discussed in this work can be transformed in a fixed-trajectory method, when neglecting in the OCP formulation of Sec. 4 the equations (54), (55) and (58), as well as the lateral acceleration control, while using the curvilinear abscissa along the race line (instead of along the centreline) as the independent variable. Alternately, one can keep the free-trajectory OCP formulation, while enforcing the lateral position constraint $n(s) = n_0(s)$, where n_0 is such that the desired trajectory is followed. The solution time of the fixed-trajectory OCP is smaller than the corresponding free-trajectory OCP – a factor around 10 is obtained in the implementation by the authors. This roughly gives a factor 100 between the typical solution time experienced with free-trajectory full-dynamic models and that of the fixed-trajectory quasi-steady OCP.

Finally, it is also possible to solve a three-dimensional fixed-trajectory OCP on the trajectory obtained from a two-dimensional free-trajectory OCP. Obviously, the resulting solution is sub-optimal, i.e. the lap time is higher, since the three-dimensionality affects the optimal trajectory. The lap-time difference depends on the vehicle/track combination. In the case of the Catalunya-Barcelona circuit, the lap-time differences are 0.2 s and 0.6 s for motorcycle and car respectively, while in the case of the Mugello circuit the differences are 0.4 s and 0.6 s, respectively.

6. Conclusion

A method to solve the minimum-lap-time of motorcycles and cars on three-dimensional tracks using quasi-steady-state models and without a pre-determined trajectory has been presented. The method builds upon g-g-g diagrams, whose main features have been discussed, namely the effect of speed, banking and slope. The method is not affected by the complexity of the vehicle model employed, because it only observes the related g-g-g diagrams. Examples of application have been given for a MotoGP bike and a Formula One car, finding that the effects of three-dimensionality as well as the speed profile and optimal trajectories are in line with those obtained in the literature with dynamic models. Therefore the method is a valid and efficient alternative to estimate the lap-time of road vehicles on closed circuits.

References

[1] Metz D, Williams D. Near time-optimal control of racing vehicles. Automatica. 1989;25(6):841–857.

[2] Gadola M, Vetturi D, Cambiaghi D, Manzo L. A tool for lap time simulation. SAE Technical Paper; 1996. Report No.: 1996-12-01.

[3] Siegler B, Deakin A, Crolla D. Lap time simulation: Comparison of steady state, quasi-static and transient recing car cornering stategies. In: of Automotive Engineers S, editor. 2000 SAE Motorsports Engineering conference amd Exposition; paper 2000–01-3563. SAE International; 2000. p. 9.

[4] Brayshaw D, Harrison M. A quasi steady state approach to race car lap simulation in order to understand the effects of racing line and centre of gravity location. Proceedings of the Institution of Mechanical Engineers, Part D: Journal of Automobile Engineering. 2005;219(6):725–739.

[5] Brayshaw D, Harrison M. Use of numerical optimization to determine the effect of the roll stiffness distribution on race car performance. Proceedings of the Institution of Mechanical Engineers, Part D: Journal of Automobile Engineering. 2005;219(10):1141–1151.

[6] Savaresi SM, Spelta C, Ciotti D, Sofia M, Rosignoli E, Bina E. Virtual selection of the optimal gear-set in a race car. International Journal of Vehicle Systems Modelling and Testing. 2008;3(1-2):47–67.

[7] Kelly DP, Sharp RS. Time-optimal control of the race car: influence of a thermodynamic tyre model. Vehicle System Dynamics. 2012;50(4):641–662.

[8] Völkl T, Muehlmeier M, Winner H. Extended steady state lap time simulation for analyzing transient vehicle behavior. SAE International Journal of Passenger Cars-Mechanical Systems. 2013;:283–292.

[9] Tremlett A, Assadian F, Purdy D, Vaughan N, Moore A, Halley M. Quasi-steady-state linearisation of the racing vehicle acceleration envelope: a limited slip differential example. Vehicle System Dynamics. 2014;52(11):1416–1442.

[10] Hendrikx J, Meijlink T, Kriens R. Application of optimal control theory to inverse simulation of car handling. Vehicle System Dynamics. 1996;26(6):449–461.

[11] Cossalter V, Da Lio M, Lot R, Fabbri L. A general method for the evaluation of vehicle manoeuvrability with special emphasis on motorcycles. Vehicle system dynamics. 1999;31(2):113–135.

[12] Casanova D, Sharp RS, Symonds P. Minimum time manoeuvring: The significance of yaw inertia. Vehicle system dynamics. 2000;34(2):77–115.

[13] Casanova D. On minimum time vehicle manoeuvring: The theoretical optimal lap [dissertation]. School of Engineering, Cranfield University; 2000.

[14] Bertolazzi E, Biral F, Da Lio M. Symbolic-numeric efficient solution of optimal control problems for multibody systems. Journal of computational and applied mathematics. 2006;185(2):404–421.

[15] Kelly DP. Lap time simulation with transient vehicle and tyre dynamics [dissertation]. Cranfield University; 2008.

[16] Bobbo S, Cossalter V, Massaro M, Peretto M. Application of the optimal maneuver methodî for enhancing racing motorcycle performance. SAE International Journal of Passenger Cars-Mechanical Systems. 2009;1(1):1311–1318.

[17] Tavernini D, Massaro M, Velenis E, Katzourakis D, Lot R. Minimum time cornering: The effect of road surface and car transmission layout. Vehicle System Dynamics. 2013;51(10):1533–1547.

[18] Tavernini D, Velenis E, Lot R, Massaro M. The optimality of the handbrake cornering technique. Journal of Dynamic Systems, Measurement, and Control. 2014;136(4).

[19] Perantoni G, Limebeer DJ. Optimal control for a formula one car with variable parameters. Vehicle System Dynamics. 2014;52(5):653–678.

[20] Limebeer DJN, Perantoni G, Rao AV. Optimal control of formula one car energy recovery systems. International Journal of Control. 2014;87(10):2065–2080.

[21] Masouleh MI, Limebeer DJN. Optimizing the aero-suspension interactions in a formula one car. IEEE Transactions on Control Systems Technology. 2016 May;24(3):912–927.

[22] Tremlett A, Massaro M, Purdy D, Velenis E, Assadian F, Moore A, Halley M. Optimal control of motorsport differentials. Vehicle System Dynamics. 2015;53(12):1772–1794.

[23] Tremlett A, Limebeer DJN. Optimal tyre usage for a formula one car. Vehicle System Dynamics. 2016;54(10):1448–1473.

[24] Dal Bianco N, Lot R, Gadola M. Minimum time optimal control simulation of a gp2 race car. Proceedings of the Institution of Mechanical Engineers, Part D: Journal of Automobile Engineering. 2017;232(9):1180–1195.

[25] Christ F, Wischnewski A, Heilmeier A, Lohmann B. Time-optimal trajectory planning for a race car considering variable tyre-road friction coefficients. Vehicle System Dynamics. 2019;0(0):1–25.

[26] Leonelli L, Limebeer D. Optimal control of a road racing motorcycle on a three-dimensional closed track. Vehicle System Dynamics. 2019;.

[27] Marconi E, Massaro M. The effect of suspensions and racetrack three-dimensionality on the minimum lap time of motorcycles. Lecture Notes in Mechanical Engineering. 2020;:1368–1377.

[28] Bianco ND, Bertolazzi E, Biral F, Massaro M. Comparison of direct and indirect methods for minimum lap time optimal control problems. Vehicle System Dynamics. 2018;0(0):1–32.

[29] Limebeer DJN, Massaro M. Dynamics and optimal control of road vehicles. Oxford University Press; 2018.

[30] Veneri M, Massaro M. A free-trajectory quasi-steady-state optimal-control method for minimum lap-time of race vehicles. Vehicle System Dynamics. 2020;58(6):933–954.

[31] Limebeer DJN, Perantoni G. Optimal control of a formula one car on a three-dimensional track—part 2: Optimal control. Journal of Dynamic Systems, Measurement, and Control. 2015;137(5):051019.

[32] Pacejka H, Besselink I. Tire and vehicle dynamics. Elsevier Science; 2012.

[33] Patterson MA, Rao AV. GPOPS-II: A MATLAB software for solving multiple-phase optimal control problems using hp-adaptive gaussian quadrature collocation methods and sparse nonlinear programming. ACM Transactions on Mathematical Software (TOMS). 2014;41(1):1.

[34] Wächter A, Biegler LT. On the implementation of an interior-point filter line-search algorithm for large-scale nonlinear programming. Mathematical Programming. 2006 Mar;106(1):25–57.

Table 1.: Motorcycle (plus rider) parameters.

Symbol	**Description**	**Value**
g	gravity	$9.81\,\mathrm{m/s^2}$
ρ_a	air density	$1.20\,\mathrm{kg/m^3}$
m	mass	250 kg
h	height of center of mass	0.69 m
h_a	height of center of pressure	0.51 m
w	wheelbase	1.50 m
b	longitudinal distance of the center of mass	0.73 m
C_DA	drag area coefficient	$0.25\,\mathrm{m^2}$
$P_{\max}$	maximum power	145 kW
μ_x	longitudinal friction coefficient	1.30
μ_y	lateral friction coefficient	1.40

Table 2.: Car (plus driver) parameters.

Symbol	**Description**	**Value**
g	gravity	$9.81\,\mathrm{m/s^2}$
ρ_a	air density	$1.20\,\mathrm{kg/m^3}$
m	mass	660 kg
h	height of center of mass	0.300 m
w	wheelbase	3.400 m
b	longitudinal distance of the center of mass	1.600 m
a	$w - b$	1.800 m
T	vehicle track	1.460 m
γ	brake ratio F_{xf}/F_{xr}	55/45
ξ	roll stiffness ratio	0.5
C_DA	drag area coefficient	$1.4\,\mathrm{m^2}$
$C_{Lf}A$	front downforce area coefficient	$2.0\,\mathrm{m^2}$
$C_{Lr}A$	rear downforce area coefficient	$2.6\,\mathrm{m^2}$
$P_{\max}$	maximum power	560 kW
p_{Dx1}	max longitudinal friction coefficient	1.75
p_{Dx2}	longitudinal friction load dependency factor	-0.175
p_{Dy1}	max lateral friction coefficient	1.80
p_{Dy2}	lateral friction load dependency factor	-0.175
N_0	nominal load (where $df_z = 0$)	2000 N